ENGINEERING

Abaxial leaf surface-mounted multimodal wearable sensor for continuous plant physiology monitoring

Giwon Lee[1,2,3], Oindrila Hossain[1], Sina Jamalzadegan[1], Yuxuan Liu[2], Hongyu Wang[2], Amanda C. Saville[4], Tatsiana Shymanovich[4], Rajesh Paul[1], Dorith Rotenberg[4,5], Anna E. Whitfield[4,5], Jean B. Ristaino[4,5], Yong Zhu[2]*, Qingshan Wei[1,5]*

Wearable plant sensors hold tremendous potential for smart agriculture. We report a lower leaf surface-attached multimodal wearable sensor for continuous monitoring of plant physiology by tracking both biochemical and biophysical signals of the plant and its microenvironment. Sensors for detecting volatile organic compounds (VOCs), temperature, and humidity are integrated into a single platform. The abaxial leaf attachment position is selected on the basis of the stomata density to improve the sensor signal strength. This versatile platform enables various stress monitoring applications, ranging from tracking plant water loss to early detection of plant pathogens. A machine learning model was also developed to analyze multichannel sensor data for quantitative detection of tomato spotted wilt virus as early as 4 days after inoculation. The model also evaluates different sensor combinations for early disease detection and predicts that minimally three sensors are required including the VOC sensors.

INTRODUCTION

The United Nations announced that 2020 is the International Year of Plant Health (IYPH), emphasizing the importance of plant health to end hunger, reduce poverty, and protect the environment. According to the Food and Agriculture Organization (FAO), it is estimated that by 2050, the productivity of food needs to be increased by about 60% to feed approximately 10 billion people all over the world (*1*). Plant diseases cause around 20 to 40% of global crop loss annually (*2*, *3*). Plant diseases not only cause notable loss in food production but also reduce species diversity, affect mitigation of people, increase control costs, and pose negative influence on human health and global food security (*1*). In this regard, sensor technologies for early disease diagnosis are essential to shorten stakeholder response time, identify threat before pathogen spreads, and reduce pesticide usage by optimizing application timing and choice of pesticides.

Tomatoes are one of the most widely consumed agriculture products (*4*). Tomato plants are susceptible to many different types of pathogens, including fungi, viruses, and bacteria, which substantially reduce the yield and quality of fruit (*5*, *6*). In addition to biotic stress, abiotic stresses such as high nighttime temperature due to climate change, mechanical damage, or inappropriate use of pesticides could also result in crucial losses of tomato yield (*7*). In this study, we choose tomatoes as a model system to design and test new sensor technologies that can monitor and predict the status of the tomato plant health and can be applied to other plants and crops.

Recently, several different sensor technologies have been developed for plant health monitoring, such as imaging and spectroscopic methods (*8*, *9*), bionanosensors (*10*), and smartphone-based devices (*11*, *12*). Imaging or spectroscopic sensors are among the few possible solutions that are capable of real-time and noninvasive monitoring. However, the imaging techniques are indirect by measuring the optical signature of the plant. Such measurement has some obvious limitations, such as poor sensitivity/selectivity and complicated processing of raw images or spectral data. Other approaches, including remote sensing (*13*) and electrophysiological sensing (*14*), have also been proposed for continuous monitoring. However, remote sensing, in general, lacks spatial solution and is not specific for particular diseases (*13*), while electrophysiological sensors have only been demonstrated for tracking water stress or the nycthemeral rhythm of the plant (*14*). Therefore, advanced sensor technologies that can track the status of plant health in real-time and dissect various biotic/abiotic stresses are needed to detect pathogens early, prevent disease outbreak, and improve plant growth and yield.

In recent years, wearable electronics have been researched widely. Applications of wearable technologies range from health monitoring (*15*, *16*), human-machine interface (*17*), to soft robotics (*18*). Wearable electronics for plant health monitoring are also emerging. These flexible sensor devices can be attached to various parts of host plants such as roots, stems, and leaves (*19*–*21*) to monitor the plant's microenvironment or physiological host responses. The physiological status of a plant is related to multiple factors. Each plant grows via a set of biological processes such as photosynthesis, transpiration, respiration, and gas exchange through the regulation of leaf epidermal pores called stomata (*22*, *23*). To accurately monitor plant health status, many of those biological processes and associated environmental conditions need to be investigated simultaneously.

Several multimodal plant wearables have been demonstrated recently for continuous plant health monitoring. Nassar *et al.* (*24*) presented a multifunctional wearable plant sensor by integrating

[1]Department of Chemical and Biomolecular Engineering, North Carolina State University, Raleigh, NC 27695, USA. [2]Department of Mechanical and Aerospace Engineering, North Carolina State University, Raleigh, NC 27695, USA. [3]Department of Chemical Engineering, Kwangwoon University, Seoul 01897, Republic of Korea. [4]Department of Entomology and Plant Pathology, North Carolina State University, Raleigh, NC 27695, USA. [5]Emerging Plant Disease and Global Food Security Cluster, North Carolina State University, Raleigh, NC 27695, USA.
*Corresponding author. Email: qwei3@ncsu.edu (Q.W.); yzhu7@ncsu.edu (Y.Z.)

temperature- and humidity-sensing functions, which was used to understand the optimal growth conditions by sensing surrounding environments. Zhao *et al.* (*25*) developed a stretchable multifunctional sensor device for detecting both microclimates (hydration, temperature, and light intensity) and growth rate of the plant. Most recently, Lu *et al.* (*19*) demonstrated a multimodal flexible sensor system for measuring microclimates (relative humidity, light intensity, and temperature) and the perception of leaf surface humidity. This device was able to detect changes in leaf surface humidity by a sensor array. However, no chemical or biological information related to the status of plant health was monitored. On the other hand, we have recently demonstrated a plant wearable sensor that can measure leaf volatile emissions and be used to diagnose plant diseases noninvasively for the first time (*26*). However, the previously developed sensor patch only detects plant volatile organic compound (VOC) signals and lacks multifunctionality. To date, a truly multifunctional and real-time sensor device that can track both biochemical (e.g., plant VOCs) and biophysical (e.g., temperature, humidity, etc.) signals of the plant and/or surrounding environments with high sensitivity and specificity has not been demonstrated yet.

In this study, we demonstrate an abaxial leaf surface-attachable multimodal wearable plant sensor patch that can continuously and simultaneously measure leaf VOCs, leaf surface temperature/humidity, and environmental humidity, with high sensitivity and selectivity. This goal was achieved with several material innovations,

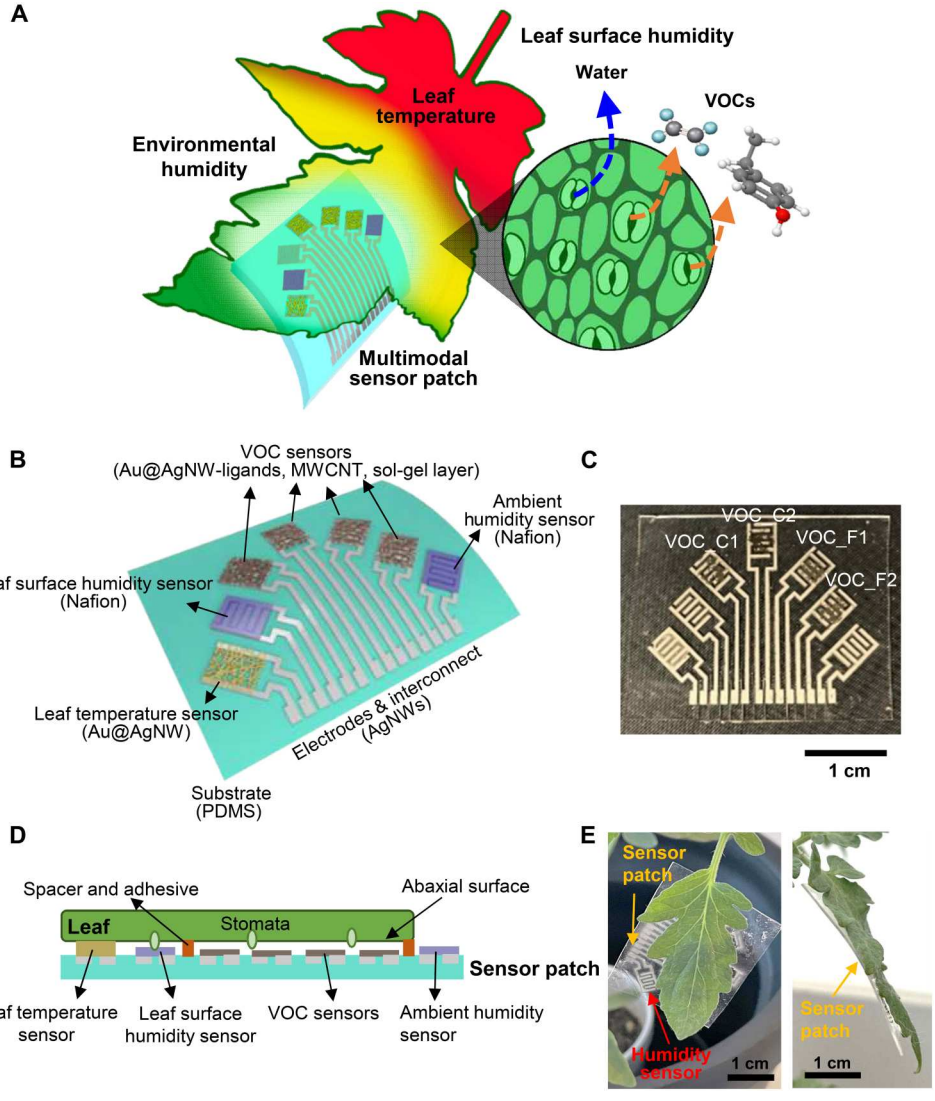

Fig. 1. A multimodal wearable plant sensor. (**A**) Schematic illustration of the sensor attached to a plant leaf. Our multimodal sensor is attached to the abaxial leaf surface to simultaneously monitor various physiology data from the leaf. Blue and orange arrows represent emissions of water and VOCs through stomata, respectively. Different colors of the leaf represent the variation of leaf surface temperature. (**B**) Overview of the wearable sensor design, which consists of four VOC sensors, one leaf surface relative humidity sensor, one leaf temperature sensor, and one environmental humidity sensor. All seven individual sensors were integrated with AgNW interconnects on a PDMS substrate. (**C**) Photograph of the actual sensor. VOC sensors with different sensing materials are labeled. (**D**) Side view of the wearable sensor patch. (**E**) Photographs of an actual sensor patch attached to the lower epidermis of the tomato leaf. The environmental humidity sensor (red arrow) is the only sensor mounted outside the leaf surface area in the air near the plant.

including the newly designed VOC sensing materials by using a network of three dimensional (3D) structured nanowire and nanotube hybrid to enable sensitive plant VOC detection in real time and gold-coated silver nanowires (Au@AgNWs) for high stability against humidity and solvent exposure. In addition, this study differs from our previous work (*26*) in several ways: (i) This new-generation wearable sensor is multifunctional, incorporating VOC, temperature, and humidity sensors for measuring both biochemical and biophysical signals of plants simultaneously. (ii) The sensor location was optimized to the lower surface of the leaf to maximize the sensor performance. (iii) This wearable device was tested on live tomato plants (cv. Mountain Fresh Plus) in both laboratory and environmentally controlled plant growth chamber environments to detect various types of stressors such as abiotic stresses (e.g., mechanical injury, drought, overwatering, salinity, and absence of light) and pathogen infections [e.g., tomato spotted wilt virus (TSWV)]. (iv) An unsurprised machine learning framework was developed to process multichannel real-time sensor data for quantitative disease assessment and prediction of the best sensor combination. To the best of our knowledge, this represents the first report of a multifunctional wearable plant sensor coupled with machine learning data analysis.

RESULTS

Design and characterization of multifunctional plant wearable sensor

Stomata are the primary gate of leaf tissues to exchange various types of molecules, including water, oxygen, carbon dioxide, and VOCs. For this reason, the plant leaf is the primary location for sensor attachment to monitor the plant biophysical properties. While many previous wearable sensors are attached to the upper surface of plant leaves (adaxial surface), our sensor patch is attached to the lower epidermis of the leaf surface (abaxial surface) to maximize the sensing capability for capturing biologically relevant targets that pass the stomata (e.g., VOCs and water molecules), which have a higher density on the lower epidermis (Fig. 1A). In addition to leaf VOCs, our wearable patch can also monitor several biophysical parameters such as leaf surface humidity, leaf temperature, and environmental humidity in parallel. To achieve this goal, the sensor patch consists of seven sensors in total, including four resistive VOC sensors, one capacitive leaf surface humidity sensor, one resistive leaf temperature sensor, and one capacitive environmental humidity sensor (Fig. 1, B and C). Among them, the leaf temperature sensor is in direct contact with the leaf surface; VOC and leaf humidity sensors face the leaf with a small gap, while the environmental humidity sensor extends from the leaf, open to the environment (Fig. 1, D and E). Active sensing materials (e.g., carbon nanotubes, Au@AgNWs, Nafion, etc.) are deposited on the as-patterned interdigitated electrodes made of AgNWs that are embedded below the surface of a soft polydimethylsiloxane (PDMS) substrate (fig. S1). The detailed sensor fabrication process is described in Materials and Methods and fig. S2.

The sensing materials for VOC detection are composed of a hybrid network of Au@AgNWs and multiwalled carbon nanotubes (MWCNTs) embedded in a hydrophobic sol-gel layer made of methyltrimethoxysilane (MTMS) and tetramethyl orthosilicate (TMOS; Fig. 2A). Both AgNWs and MWCNTs have a high aspect ratio that can maintain the percolation state under deformation of those materials. Moreover, these materials are highly conductive, stable, and easy to process because of their well-established chemistry properties. Synthesized Au@AgNWs were characterized with a transmission electron microscope (TEM) and an energy-dispersive spectrometry (EDS) detector, as shown in Fig. 2B. Compared to bare AgNWs, Au@AgNWs have a thin gold layer (~30 nm) on the surface, enabling reaction with thiolated surface ligands. Moreover, the gold coating on AgNWs can improve stability under various chemical environments (*27*). The Au@AgNWs were coated with various halothiophenol ligands [e.g., fluorothiophenol (FTP), chlorothiophenol (CTP), bromothiophenol (BTP), and iodothiophenol (ITP)] to selectively detect leafy aldehydes through reversible halogen bonding (Fig. 2A) (*26*). The surface modifications were characterized with ultraviolet-visible (UV-vis) spectroscopy to optimize the surface ligand density (fig. S3). The Au@AgNWs created a rough 3D surface layer that greatly increased the effective sensor surface area for VOC capturing (Fig. 2C and fig. S6). As shown in Fig. 2C, ligand-functionalized Au@AgNWs were further wrapped and interconnected with MWCNTs because of the size and modulus differences between the two materials, which together formed a robust heterogeneous sensing network. On top of these active sensing materials, a hydrophobic and nanoporous sol-gel layer was uniformly coated by drop casting (fig. S4). The water contact angle of the sensing film was 82° and 111° before and after the sol-gel coating, respectively (fig. S5). We also measured scanning electron microscopy (SEM) images with top and cross-sectional views to investigate the morphology of the VOC sensing composite materials coated with the sol-gel layer (fig. S6). The sol-gel coating substantially increases the mechanical stability of the VOC sensor, reduces cross-talk to humidity interference (Fig. 2F), and also minimizes sensor baseline drift (fig. S7), which will be discussed in more detail later.

We then tested the performance of the VOC sensors (namely, FTP, CTP, BTP, and ITP sensors) by measuring the electrical resistance under the exposure of acetone or hexanal vapors, which are used to mimic ketone and aldehyde-based VOCs emitted from the plant (Fig. 2, D and E, and fig. S8) (*28*). The VOC sensors are operated as chemiresistive sensors, where the electrical resistance of MWCNTs varies upon the attachment of VOC molecules on their surface, which creates a doping effect on the carbon nanomaterials (*29*). When solvent vapor concentration was reduced from 500 to 100 parts per million (ppm), the sensor response ($\Delta R/R_0$) decreased accordingly, as a result of the reduced interaction between VOC gas and sensing materials (Fig. 2, D and E). Furthermore, for both acetone and hexanal vapors, the sensitivity of FTP and CTP sensors is the highest among the four, followed by BTP and ITP sensors. This is due to the decreasing electronegativity of the halogen atoms, following the order of F > C > B > I. For the final wearable sensor patch, only FTP and CTP VOC sensors (termed VOC_F and VOC_C, respectively) were integrated because of their higher detection sensitivity.

To characterize the potential cross-talk from other stimuli such as humidity and temperature, the VOC sensors were tested under different humidity and temperature conditions. As shown in Fig. 2F, the presence of a hydrophobic and gas-permeable sol-gel layer on the top of the VOC sensors can prevent the interference of water molecules up to 90% relative humidity (Fig. 2F, black curve), whereas the control sensor without the sol-gel coating showed a clear response to the environmental humidity (Fig. 2F,

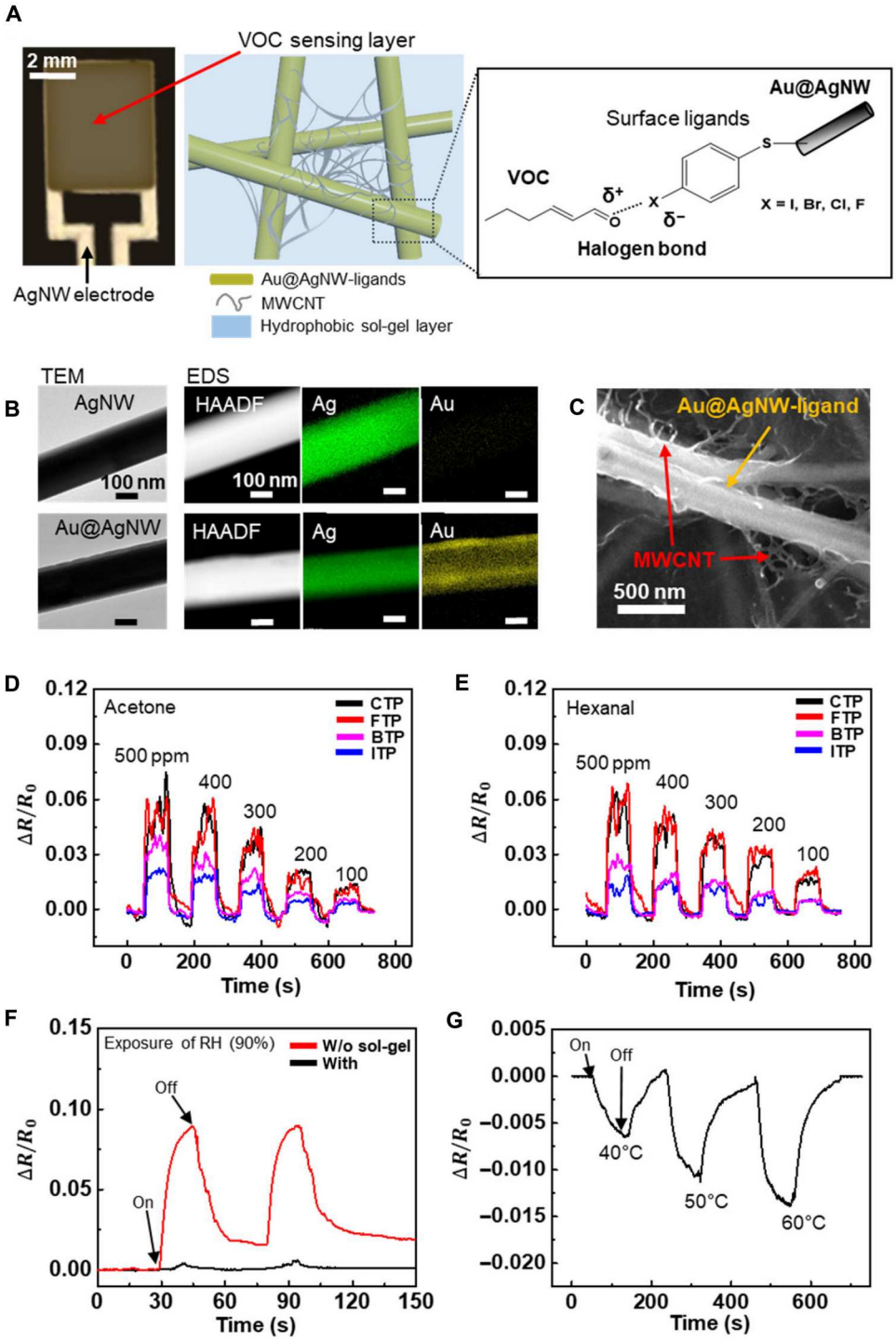

Fig. 2. Characterization of VOC sensors. (**A**) Optical photograph of VOC sensor and schematic of the sensing materials. Au@AgNWs with surface ligands and MWCNTs were covered with a hydrophobic sol-gel layer. Surface ligands are halothiophenols immobilized on the gold surface, which selectively interact with leaf aldehydes. (**B**) TEM and EDS images to compare the morphology of AgNWs and Au@AgNWs. (**C**) SEM image of the Au@AgNW and MWCNT composite showing MWCNTs were wrapping on the Au@AgNW surface. (**D** and **E**) Electrical resistance changes of different surface ligand–functionalized VOC sensors (e.g., FTP, CTP, BTP, and ITP) under exposure of (D) acetone and (E) hexanal, respectively. Vapor concentrations are theoretical concentrations at the nozzle tip of the gas-mixing system. (**F**) Humidity interference test of the VOC sensor with or without the sol-gel layer. The hydrophobic sol-gel layer prevents interaction of water molecules with the VOC sensor. (**G**) Temperature interference test of the VOC sensor. HAADF, high-angle annular dark-field.

red curve). The sol-gel layer also improved the repeatability of the VOC sensor response by enhancing the stability of the sensing materials on PDMS substrate and reducing baseline signal drifting (fig. S7). For temperature interference, the VOC sensor showed minimal dependence on the external temperature (Fig. 2G), owing to the opposite temperature coefficient of resistance values of MWCNTs (−0.33%/K) (*30*) and AgNWs (0.26%/K; fig. S9) (*31*). Although the resistance of VOC sensors slightly fluctuated with the temperature variation (from 40° to 60°C), this change was less than 0.7% for 40°C and lower temperatures (Fig. 2G), exhibiting acceptable temperature stability for real plant applications.

Figure 3A shows the sensing performance of the leaf temperature sensor, composed of as-synthesized Au@AgNWs (without functionalization) as the sensing agent. Because of the temperature sensitivity of Au@AgNWs and the thermal expansion of PDMS substrate, the nanowire-based temperature sensor can detect temperature changes from room temperature to 60°C. To investigate the effect of PDMS thermal expansion on temperature sensing, we varied the elastic modulus of PDMS by tuning the mixing ratio of prepolymer and curing agent from 5:1 to 20:1 (Fig. 3A). As the mixing ratio increased to 20:1 (resulting in softer PDMS), the sensitivity of the temperature sensor slightly increased because of larger thermal expansion of PDMS, which decreased the percolation between Au@AgNWs (*32*). Moreover, the interference of different humidity levels or solvent exposure to the temperature sensor was also examined (Fig. 3B). The slope of each response curve did not change obviously when various humidity levels (relative humidity, 25, 50, and 75%) or 500 ppm of acetone were applied, indicating the excellent stability of the temperature sensor. These results can be explained by the protective effect of the gold layer on the AgNW core, which does not interact with water or common VOC vapors because of its chemical inertness.

The performance of the humidity sensors was also characterized. In this case, Nafion film was used as the active humidity sensing material by measuring its capacitance changes between two electrodes. The thickness of the Nafion film was controlled to optimize the detection sensitivity (Fig. 3C). Nafion is known to absorb water molecules, resulting in an increase in the capacitance value by replacing air with water molecules within the film (*33*). As the thickness of the film was increased, the sensitivity was enhanced because of the higher capacity of absorbing water molecules (Fig. 3C). However, when the thickness was above 5 μm, the film was delaminated from the substrate because of a larger stiffness mismatch between the film and the substrate (*34*). Therefore, a 2-μm-thick Nafion layer was selected as the optimized thickness. To test the cross interference, we applied various temperatures (10°C, room temperature, and 40°C) or 500 ppm of acetone vapor to the humidity sensor (Fig. 3D). With the increase of temperature, larger thermal movement of water molecules would induce higher polarization, resulting in a larger capacitance (*35*). This means that the absolute capacitance value (C) would change as a function of the temperature. However, the relative capacitance response ($\Delta C/C_0$) is quite consistent for temperatures between 10° and 40°C. In the case of acetone exposure, the sensitivity of the humidity sensor was reduced slightly because of water molecule absorption in the presence of acetone. We also compared the sensor performance against previously published multifunctional wearable sensor patches, which demonstrated that our sensor platform is one of the few that can detect biochemical and physical parameters in parallel (table S1).

Abaxial leaf surface attachment

Next, the influence of the sensor location, namely, the adaxial (upper surface of leaf) attachment versus the abaxial (lower surface of leaf) attachment, was evaluated on a live tomato plant. In Fig. 3E, the photographs show that the sensor can be directly attached to the backside of the leaf. The difference in stomata density between the adaxial and abaxial surfaces of the leaf was observed via bright-field optical microscopy (Fig. 3F and fig. S10). As shown in Fig. 3G, the density of stomata on the abaxial surface is approximately 73% higher than that of the adaxial leaf. This result agrees with the previous study, where a higher density of stomata on the lower surface of tomato leaf was reported (*36*). Moreover, we compared various sensor responses from adaxial and abaxial leaf surfaces (fig. S11). For leaf surface humidity and VOC sensors, the sensor responses with abaxial surface position were, on average, 10 to 20% higher than those of adaxial surface (Fig. 3H). Here, the leaf surface humidity sensor measured the leaf-emitted water under normal growth conditions, while the VOC sensor signal was induced by the leafy VOC profile change upon mechanical leaf cutting. The signal difference was attributed to the difference in stomata density between the upper and lower surfaces of the leaf (Fig. 3G). For better sensor performance, we therefore chose the abaxial epidermis of the leaf as our sensor attachment location for the rest of the experiments in this work. In addition, we tested the wearability and biocompatibility of sensor for nearly 3 weeks on a live tomato plant. The data showed no apparent indication of plant stress after sensor attachment (fig. S12).

Before testing the plant stress conditions in the next section, we first monitored the leaf surface temperature and relative humidity of a healthy tomato plant during sunny and rainy days continuously using the wearable sensor patch (Fig. 3I). As the light intensity increased during the daytime, the leaf surface humidity signals reached the maximum in the middle of the day because of the increased number of open stomata to release the water molecules to the environment (Fig 3I). This indicates that the intensity of the sunlight can modulate the opening of stomata on leaf surface (*37*). The leaf temperature increased under the sunlight condition during the daytime, followed by a decrease in temperature that is attributed to the enhanced leaf transpiration (Fig 3I and fig. S13). However, such a circadian rhythm was much less obvious during rainy days when the plant was less influenced by the sunlight with high relative humidity of the air (Fig 3I). The reading error of the wearable humidity sensor was within 10% when compared to a commercial environmental sensor (table S2). These results show that this multimodal sensor patch can be potentially used for the study of plant chronobiology in addition to disease and stress detection as described below.

Monitoring abiotic stresses on tomato plants

To demonstrate the usability of the multimodal sensor, the patch was mounted on a live tomato plant for monitoring various abiotic stresses, including drought, overwatering, salinity, and darkness (Fig. 4). Figure 4A shows the schematic illustration of the experimental setup. Four stressors were introduced sequentially to the same tomato plant wearing the sensor patch to minimize host difference. For this experiment, we used a multimodal wearable sensor

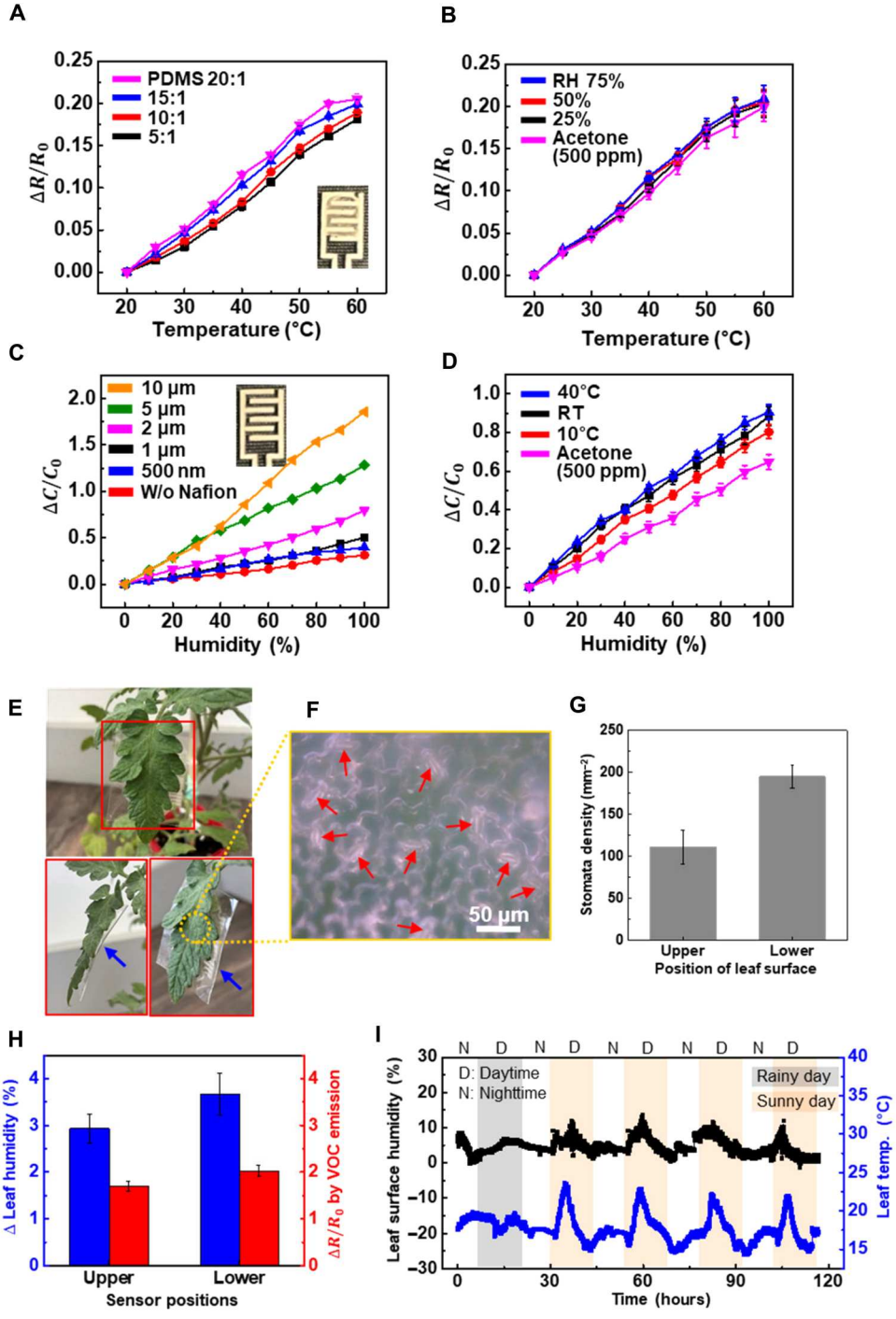

Fig. 3. Characterization of temperature and humidity sensors. (**A**) Resistance changes under increasing temperature with various mixing ratio of PDMS (error bar represents $n = 3$ measurements). The inset is an optical image of the actual temperature sensor. (**B**) Humidity and vapor interference tests for the temperature sensor. The temperature response was measured under relative humidity (RH) of 25, 50, and 75% or in the presence of 500 ppm of acetone vapor (error bar represents $n = 3$ measurements). (**C**) Capacitance changes under increasing humidity with various thickness of Nafion film. The inset is a photo of the actual humidity sensor. (**D**) Temperature and vapor interference tests for the humidity sensor. The humidity was measured at diverse temperatures [10°C, room temperature (RT), and 40°C] or in the presence of 500 ppm of acetone vapor (error bar represents $n = 3$ measurements). (**E**) Photographs of the sensor attached underneath the leaf. Front view (top row) and side views (bottom row). Blue arrows indicate the sensor. (**F**) Optical microscopy image of the stomata on the abaxial tomato leaf surface. Red arrows indicate the presence of stomata on the abaxial leaf surface. (**G**) Comparison of stomata density between the upper and lower surface of the leaf. Error bars are SDs from five samples. (**H**) Output signal differences of leaf surface humidity and VOC sensor with different sensor attachment positions. Error bars are SDs from five samples. (**I**) Real-time monitoring of leaf surface relative humidity and leaf surface temperature of a healthy tomato plant. D and N represent the daytime and nighttime, while gray and carnation colors indicate rainy day and sunny day, respectively.

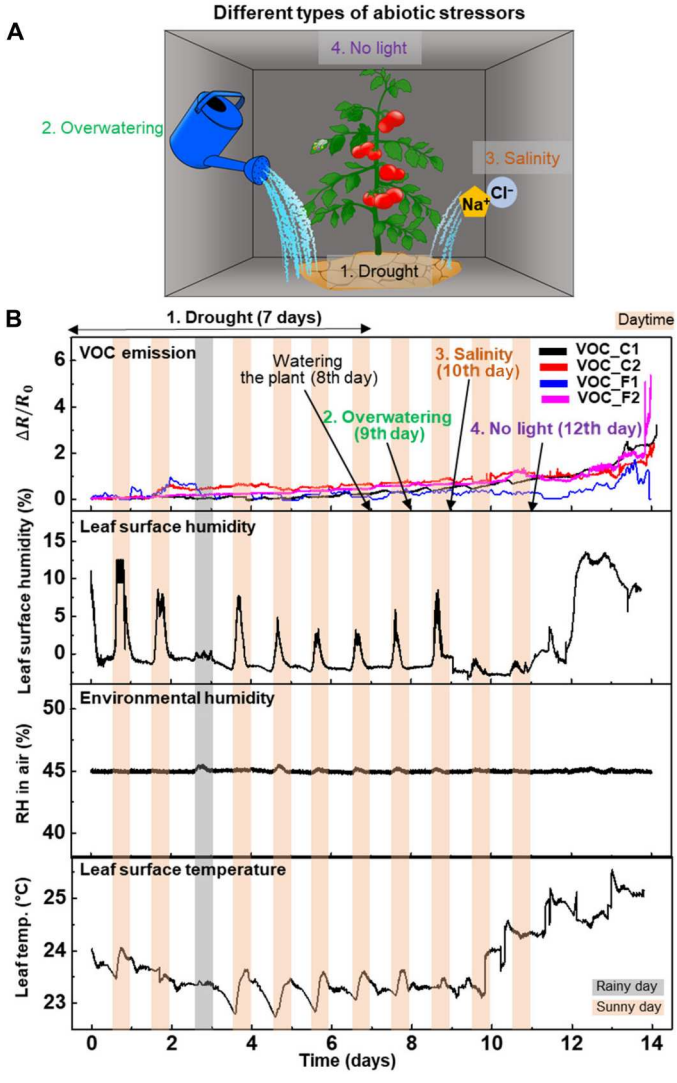

Fig. 4. Plant wearable for monitoring abiotic stresses. (**A**) Schematic illustration of the experimental setup for sequential abiotic stress monitoring, including drought, overwatering, salinity, and no light. (**B**) Real-time sensor data from the same tomato plant exposed to various abiotic stresses. VOC_C1 and C2 correspond to CTP sensors, while VOC_F1 and F2 are FTP sensors. Black arrows represent specific times for applying different conditions. Carnation color indicates the daytime of measurement. Gray color represents the rainy day.

composed of four VOC sensors (CTP sensors: VOC_C1 and C2; FTP sensors: VOC_F1 and F2), one leaf surface humidity sensor, one environmental humidity sensor, and one leaf surface temperature sensor. By applying the sequential stimuli, the responses of the sensor with multiple electrical signals were simultaneously monitored by a multichannel data recorder for up to 14 days (Fig. 4B). First, watering was prevented for 7 days to mimic a drought environment. In this stage, the leaf surface humidity gradually reduced as water was conserved inside the plant over time, while the VOC signals increased slightly (Fig. 4B, first and second panel). Although the plant was grown indoors, we were able to capture a rainy day (day 3) by observing the depression of leaf transpiration that was modulated by the different lighting conditions, similar to the results in Fig. 3I. After 7 days, the plant was watered normally to reduce the water stress, and the plant recovered for another day before the next experiments. On day 9, excessive water was applied to create an overwatering condition. Immediately, the surface humidity of the leaf increased about 1.5 times as water content inside the host decreased as increased water evaporation occurred through the leaf surface (Fig. 4B, second panel). On day 10, salinity stress was introduced by using 150 mM salted water. Typically, under high-salt conditions, the transpiration of the plant would be reduced because of the reduction of water absorption from roots as a result of the osmotic pressure difference between soil and root (*38*). This was confirmed from our experimental data, where the suppression of leaf surface humidity change and rapid increase of leaf temperature due to reduced transpiration was observed (Fig. 4B, second and fourth panel). For the last experiment (day 12 and after), the plant was placed in complete darkness by covering the plant with a box. In this case, notably increased VOC emission, leaf surface humidity, and leaf temperature were observed, which probably resulted from the induced stress due to the lack of photosynthesis. The plant eventually died at the end of the experiment while showing high levels of VOC emissions and increased leaf temperature. The elevated leaf surface humidity after light blocking appears contradictory to the conventional plant physiology theory. However, we attribute this phenomenon to the plausible evapotranspiration effect of a dying plant. To validate our results, we also repeated the abiotic stress experiments with single stressors (one stress at a time), and the plant responses were recorded by both wearable sensors (figs. S14 to 17) and a commercial leaf porometer (figs. S18 and S19). Both devices showed good agreement with each other. Briefly, the shortage and excessive watering moderately decreased or increased the stomatal conductance and leaf surface humidity, respectively (fig. S19 and table S3). Watering with high salt concentration inhibited the transpiration because of the imbalance of the osmotic pressure in roots (fig. S19 and table S3). Last, blocking the light hindered the photosynthesis process and therefore resulted in the reduction of leaf surface humidity and temperature (fig. S19 and table S3). Each stress was measured three times, and their sensor response trend was summarized in table S3.

In addition, we also monitored the plant response to mechanical damage on leaves by the wearable sensor patch (fig. S20). When cutting or detaching the leaf, the VOC sensors detected more obvious and immediate response signals than other sensors (e.g., temperature and humidity sensors; fig. S20), indicating that the biochemical sensor was more sensitive than biophysical sensors in the detection of acute plant tissue damages.

Monitoring biotic stress and early pathogen detection

Next, we tested the wearable sensor patch for monitoring different pathogens on live tomato plants. TSWV (a viral pathogen) and early blight (*Alternaria linariae*, a fungal pathogen) were selected because of their prevalence in tomato production (fig. S21) (*1*, *39*, *40*). As shown in fig. S22, the experiments were conducted in a growth chamber at the North Carolina State University (NCSU) Phytotron, maintained at a constant 23°C with a 16-hour photoperiod and constant carbon dioxide concentration (400 ppm). TSWV inoculation was first performed, and the plant response was monitored by the wearable sensor. By measuring the electrical signals with the wearable sensor, differentiable VOC signals can be seen after

around 5 days post inoculation (dpi; inoculated on day 4 and detectable VOC signals on day 9; $n = 3$ replicated measurements; Fig. 5A and fig. S23). To compare our electrical sensing method with the conventional molecular diagnostic method, a TSWV-specific real time reverse-transcription loop-mediated isothermal amplification (RT-LAMP) assay was performed in parallel (Fig. 5B and Materials and Methods). According to the real-time RT-LAMP assay results, successful inoculation of the plant generated consistent positive nucleic acid test results 7 dpi (Fig. 5B), which is later than the wearable sensor patch. More quantitative early detection data were determined by the machine learning analysis described below. In addition, a rapid change of VOC signals and a decrease in leaf

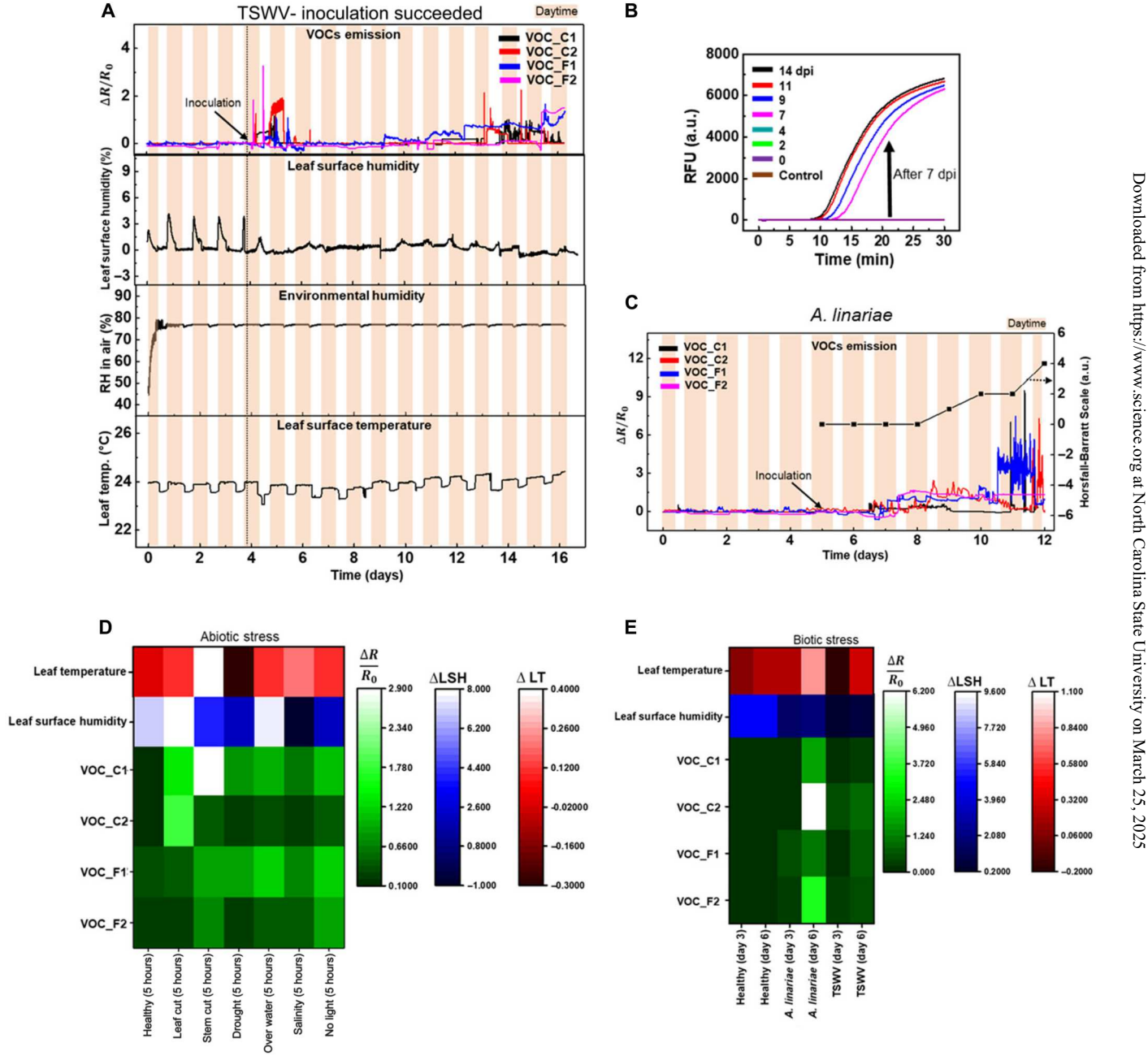

Fig. 5. In-situ measurement of tomato plant health under biotic stresses (pathogen infections) in phytotron. (**A**) Real-time wearable sensor data of a live tomato plant after TSWV inoculation. VOC_C1 and C2 correspond to CTP sensors, while VOC_F1 and F2 are FTP sensors. Black arrows represent specific time for conducting the inoculation. Carnation color indicates the daytime of measurement. (**B**) Real-time LAMP assay results, verifying the presence of TSWV pathogens after different days of inoculation. After 7 dpi, a positive result was detected by the RT-LAMP assay for three of four plants. (**C**) Wearable VOC sensor data and the conventional Horsfall-Barratt scale (black line) for the inoculation experiment with *A. linariae*. Heatmap of sensor data after 5 hours of different abiotic stresses (**D**) and heatmap of sensor data on days 3 and 6 of the tomato plant with various pathogens (**E**). $\Delta R/R_0$, ΔLSH, and ΔLT represent the resistance change due to leaf VOC emission, leaf surface humidity variation (LSH), and leaf temperature (LT) change, respectively. a.u., arbitrary units.

surface relative humidity was captured right after the inoculation (days 4 and 5). These signal perturbations were attributed to the mechanical damage to the leaf surface during the TSWV rub-inoculation process. The VOC signals returned to the baseline on day 7, indicating the recovery of the plant from mechanical damage. In addition to VOCs, leaf surface relative humidity rapidly decreased and the leaf temperature slightly increased after inoculation [Fig. 5A (second and fourth panel) and fig. S23], which can be related to the mechanical damage of the leaf surface and also the closure of the stomata after pathogen infection (*41*). When a plant is infected by TSWV, stomata generally close as a result of invasion by the pathogen, resulting in a lower transpiration rate (*42*). Although less specific, these biophysical signals (e.g., leaf surface relative humidity and temperature) are easy to monitor compared to VOC signals and hence could be useful plant health indicators on their own.

Monitoring host plant response using the patch sensors also allowed us to determine whether inoculations were successful. Failed inoculations resulted in response patterns that varied widely from successful inoculations that developed into visible symptoms (fig. S24). In the case of mock inoculation, the VOC signals did not increase after 5 dpi (fig. S24). The rapid increase of VOC signals immediately after the inoculation was still observed, confirming that this instant VOC response is indeed induced by mechanical damage to the leaf. Furthermore, during the entire period, both leaf surface relative humidity and temperature remained mostly constant, which also indicated that the plant was not infected by TSWV. The unsuccessful inoculation was lastly confirmed by the RT-LAMP assay (fig. S25).

To demonstrate the feasibility of detecting fungal pathogen infection using the same sensor patch, we also performed inoculation experiments with *A. linariae* (n = 3 replicated measurements; Fig. 5C figs. S26 and S27). Because the inoculation of this fungal pathogen was performed by spraying the pathogen solution on the leaf surface without mechanical damage, no instant VOC signal changes were observed after inoculation in this case (Fig. 5C and fig. S27). For *A. linariae*, our wearable sensor demonstrated the capability of detecting pathogen infection before the visual assessment method. Conventionally, the visual symptoms were quantified using the Horsfall-Barratt scale for assessing disease severity (table S4) (*43*). On the basis of the scale, the infection could be confirmed visually 4 dpi for *A. linariae* (Fig. 5C, black squares). However, the wearable VOC sensor was able to capture elevated VOC emissions after 2 days of infection, approximately 2 days before the visible assessment method. Leaf surface humidity and temperature signals also showed different patterns before and

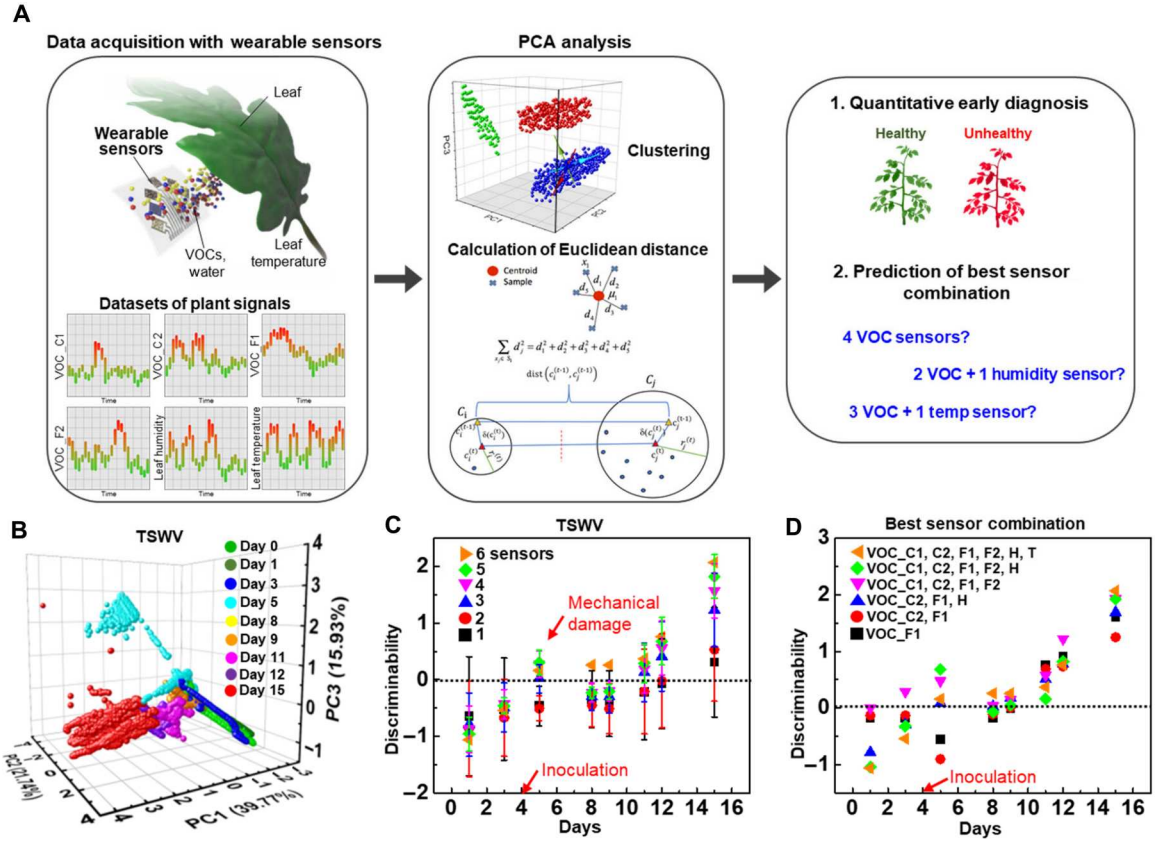

Fig. 6. Machine learning analysis of the real-time TSWV sensor data. (**A**) Schematic diagrams of the process of machine learning using PCA method. (**B**) A representative graph showing 3D PCA analysis from days 0 to 15 for the six-sensor combination (VOC_C1, C2, F1, F2, H, and T). VOC_C1, C2, F1, F2, H, and T denote four VOC sensors, leaf surface relative humidity sensor, and leaf temperature sensor, respectively. (**C**) Average discriminability values with different numbers of sensors as a function of infection days. Error bars represent the SDs of each number of sensors. (**D**) Discriminability with the best sensor composition for each number of sensors. VOC_C1, C2, F1, F2, H, and T denote four different types of VOC sensors, leaf surface relative humidity sensor, and leaf temperature sensor, respectively.

after infection (figs. S26 and S27). Together, these results (Fig. 5, A and C) suggested that the wearable sensor technology was able to detect different kinds of plant pathogens (viral and fungal) 2 to 3 days earlier than conventional detection methods, such as the nucleic acid testing by LAMP assays (Fig. 5B) and the visible inspection in Fig. 5C. Our previous work also demonstrated that the wearable sensor could detect infection by the oomycete pathogen *Phytophthora infestans* (*26*). As a comparison, healthy tomatoes sprayed with water instead of the spore solution showed no sensor response at all (fig. S28).

Moreover, by combining all the sensor signals, the wearable sensor patch was capable of distinguishing biotic stress from abiotic factors such as mechanical cutting, drought, overwatering, salinity, and light deficiency. To demonstrate that, heatmaps were generated using the sensor data at specific time points for differentiating all abiotic and biotic stresses that have been screened. As shown in Fig. 5D, the VOC, leaf surface relative humidity, and temperature data were combined and depicted with different color scales. Distinct electrical responses of the plant wearable sensor under different abiotic stresses can be seen after a constant exposure time period of 5 hours. Moreover, similar to the case of abiotic stress, all three tested pathogens could be discriminated from each other and also from the healthy plants by using the same sensor patch through the combination of the sensor signals (VOC, leaf temperature, and humidity) at specific time points (e.g., days 3 and 6; Fig. 5E). Such a distinct sensor pattern could be recognized and classified by machine learning methods in the future for rapid differentiation.

Machine learning for quantitative early detection and prediction of best sensor combination

To quantitatively assess our multimodal sensors for the early detection of pathogens, an unsupervised machine learning approach based on principal components analysis (PCA) was used to analyze the real-time sensor data (Fig. 6) (*44*, *45*). PCA is one of the most well-known statistical algorithms in data analysis and image processing projects for multivariate variable dimensionality reduction with impactful benefits such as feature selection and event classification. In comparison with other conventional methods such as t-distributed stochastic neighbor embedding (t-SNE), the PCA approach is more applicable in multivariable sensor systems (*46*). Figure 6A depicts the schematic illustrations of the PCA-based data analysis pipeline for processing real-time sensor data. For the demonstration, we used the TSWV inoculation data (Fig. 5A) as an example. The multichannel wearable sensor data from the same plant was first divided into different days (e.g., days 0, 1, 2, 3, etc.). Day 0 data were used as the healthy control and compared to other days. Data from different days were clustered by PCA with reduced data dimensions. Then, the centroid and Euclidean distance between two centroids of clusters (two different days) were calculated (see details in Materials and Methods). The separation of the clusters was quantitatively assessed by a parameter called "discriminability" (D), as defined by the following equation

$$D = E - (R_{STD,1} + R_{STD,2})$$

where D, E, and R denote discriminability, Euclidean distance, and radius (or SD) of the cluster, respectively.

As shown in Fig. 6B, a three-component PCA for a total of six sensors [namely, VOC_C1, VOC_C2, VOC_F1, VOC_F2, leaf surface relative humidity sensor (H), and temperature sensor (T)] from days 0 to 15 shows the gradual separation of sensor signals from day 0 (green dots) throughout the TSWV infection process. In the early days, the most obvious cluster separation occurred on day 5 (cyan dots) because of the mechanical damage induced by the inoculating method (Fig. 6B). All PCA data with other sensor combinations (e.g., five sensors, four sensors, three sensors, etc.) are also shown in fig. S29.

Using discriminability (capturing different signal changes), we are able to quantitatively differentiate diseased plants from healthy controls and determine the accurate early detection day. Simply, if the discriminability value is positive, the two sensor clusters are considered distinguishable, resulting in a positive diagnosis result. On the other side, if the value is negative, that means the two clusters under comparison are overlapped, resulting in a negative detection result. We applied the PCA to all possible sensor combinations using six individual sensors (total 63 combinations) and calculated discriminability for each sensor combination (Fig. 6C and fig. S30). Figure 6C shows the averaged discriminability value for each sensor combination, and the SD represents the different performance when the number of sensors is fixed but the sensor composition is different. On the basis of the data, it clearly suggests that the more sensor channels that were used, the higher the discriminability value, which also means higher confidence in a positive detection. Excluding the day 5 data (positive but mainly because of mechanical perturbation), the six-sensor channel combination can clearly detect TSWV infection as early as day 8, which is 4 dpi, much earlier than the RT-LAMP results (7 dpi; Fig. 5B). Figure 6C displayed a large error bar for each fixed number of sensors, suggesting that the actual sensor channel combination is equally if not more important to the total number of sensors. The best combination for each number of sensors is presented in Fig. 6D. According to the discriminability values, a minimum of three sensors (VOC_C2, VOC_F1, and H) is needed for the early detection of TSWV after 4 dpi (Fig. 6D, blue triangle). In addition, the results suggest that for effective disease detection, the biochemical VOC sensor is probably the most important sensor that is needed in each sensor combination; in addition, the leaf surface humidity sensor works slightly more effectively than the leaf temperature sensor in disease detection (Fig. 6D). Such a machine learning analysis can help find the most impactful sensor (and sensor combination) for a particular application and potentially reduce the total number of redundant sensors, which would be particularly useful to reduce sensor cost while maintaining sensor performance.

DISCUSSION

Multifunctional and miniaturized sensor technology for continuous plant physiology monitoring is of great interest for early disease detection, stress sensing, and growth prediction. However, many existing wearable sensor technologies can only detect physical growth of the plant or environmental parameters of the atmosphere (table S1). None of these sensor platforms has been developed to monitor multiple signals that can inform plant health. Here, a multimodal plant wearable sensor patch capable of detecting both biochemical and biophysical parameters of individual plants, namely, leafy VOCs, leaf surface humidity, leaf surface temperature, and

environmental relative humidity, was demonstrated for continuous, on-plant physiology monitoring. This versatile device used a newly designed 3D nanohybrid sensing network to capture leaf VOC signals and greatly minimized the cross-talk between VOC, temperature, and humidity signals. The performance of each sensor component integrated on the patch (e.g., detection sensitivity and range) matches well with what has been demonstrated in the existing multiplexed sensor platforms and has room to approach those monofunctional sensors (table S1). Moreover, our sensor was mounted underneath the leaf surface (abaxial surface) to maximize the output signals from the plant, which is different from many previous sensor applications. With this multimodal sensor patch, we demonstrated the monitoring of various types of plant stresses from drought, overwatering, salinity, light deficiency, mechanical damage, and pathogenic infection (virus and fungus) in both laboratory and greenhouse conditions. In particular, the wearable sensor patch demonstrated capability for the early detection of plant pathogens (2 to 3 days earlier) when compared to conventional nucleic acid LAMP-based reactions or visual assessment techniques.

In addition, a machine learning analysis framework based on the PCA approach was developed to quantitatively determine the early detection capability and screen the best combination among multiple sensors. In recent years, applying machine learning approaches such as supervised and unsupervised learning have been greatly increased in the biosensor area because of their outstanding benefits in data analysis and noise reduction. Specifically, integrating machine learning with biosensors for plant disease detection, stress phenotyping, and predictive analysis showed meaningful results (*47*). In this research, we conducted PCA as one of the most common unsupervised machine learning algorithms to reduce the dimensions of multichannel sensor data and also classify the roles of each sensor in combination to find out the best combination candidates to predict plant disease sooner. This data analytics–coupled sensor platform could be used for various applications related to plant health monitoring and crop loss prevention in agricultural settings.

For practical field applications, the size of sensor patches should be further miniaturized using higher-resolution fabrication techniques such as photolithography, micromolding in capillaries (even on curved surfaces) (*48*), or direct laser writing (*49*). The geometry of sensor patch also needs to be flexible to fit diverse shapes of attaching leaves. In multimodal sensors, cross-sensitivity inhibits the precise measurement of a specific target when multiple stimuli are present at the same time. Therefore, it is critical to implement decoupled sensing mechanisms such as different sensing materials, sensor layouts, and signaling principles in future sensor design and development (*50*). Moreover, a fully standalone sensor device will be expected in the future, which requires the integration of other essential components such as thin-film batteries, self-powered units (*51*), and functional circuits (*52*) for wireless signal transmission with the sensing elements on the same patch. The robustness of the sensor patch will also need to be thoroughly tested in the greenhouse and field trails.

MATERIALS AND METHODS

Materials and reagents

All materials and reagents were used without further purification. MWCNTs, Nafion, hexanal, and acetone were purchased from Sigma-Aldrich. PDMS (SYLGARD 184) was purchased from Dow Corning.

Synthesis of nanowires

The Au@AgNWs were synthesized by a modified chemical solvent method based on the previously reported procedure (*27*). The AgNWs are prepared by a modified polyol method and dispersed in deionized (DI) water for the following steps (*53*).

For the preparation of solution A, 10 ml of AgNW aqueous solution (10 mg/ml), 70 ml of 5 weight % polyvinylpyrrolidone aqueous solution (M_w, 40,000; Sigma-Aldrich), 14 ml of 0.5 M L-ascorbic acid aqueous solution (Sigma-Aldrich), 14 ml of 0.5 M sodium hydroxide (Sigma-Aldrich), 3.5 ml of 0.1 M Na_2SO_3 (Sigma-Aldrich) aqueous solution, and 80 ml of DI water were uniformly mixed with a glass rod. The prepared solution was denoted as solution A.

For the preparation of solution B, 10 ml of 0.1 M sodium sulfite aqueous solution, 3.5 ml of 0.5 M sodium hydroxide aqueous solution, and 100 ml of DI water were mixed first. Then, 1.5 ml of 0.25 M hydrogen tetrachloroaurate(iii) hydrate aqueous solution ($HAuCl_4{\cdot}xH_2O$; Sigma-Aldrich) was added to the mixed solution. The solution was then stirred gently with a glass rod. The prepared solution is denoted as solution B.

Solution B was then immediately but slowly poured into solution A to produce a mixture that appeared light purple with a metallic gloss. Then, the beaker of the mixed solution was sealed and left for 12 hours. After the reaction, the Au@AgNWs turned light brown and precipitated out of the solution. The remaining solution turned clear black. These nanowires were then collected and washed with 95% ethanol three times using centrifugation (1000 rpm for 1 min) and dispersed in ethanol for further use.

Preparation of VOC sensors

The VOC sensor′s performance depends heavily on the amount of ligands attached to the surface of the nanomaterials. To optimize the concentration and the amount of ligands decorated to the surface of Au@AgNWs, four different concentrations (0.01, 0.1, 1, and 10 μM) of FTP ligands were tested. We found a higher tendency of agglomeration of the nanowire solutions at the higher ligand concentration. However, if the amount of surface ligand is too low, then the reactivity toward VOC analytes will also be reduced. Therefore, 0.1 μM ligand solutions were eventually chosen to functionalize Au@AgNWs without notable aggregation. After that, we optimized the amount of ligand solutions by changing the volume of ligand solutions (e.g., 300, 500, and 1000 μl). The 500-μl solution was selected to balance the ligand density and nanomaterial stability. Similarly, 500 μl of 100 nM ITP, BTP, and CTP ligand solutions were used to prepare other VOC sensors. Every functionalization reaction was continued for 8 hours with slight shaking at room temperature. The supernatant was then collected to measure their UV-vis spectrum. After that, ligand-attached Au@AgNW solutions were added to MWCNTs at a 5:1 mixing weight ratio.

The sol-gel film was prepared by mixing MTMS, TMOS, methanol, and Nanopure water in the molar ratio of 1:1:11:5. The solution was stirred at room temperature for 2 hours. The final formulation was diluted 10 times by adding methanol before drop-casting.

Fabrication of a multimodal wearable plant sensor

As shown in fig. S2, AgNWs were spray-coated on the polyimide (PI) substrate using a stencil mask for patterning interdigitated electrodes and interconnect. After patterning, PDMS solution was poured to transfer AgNWs from PI to PDMS. The PI substrate was removed when the PDMS was fully cured. With a patterned AgNW substrate, sensing materials for each sensor (e.g., Au@AgNWs for temperature sensor, Nafion for leaf surface humidity sensor and environmental humidity sensor, and functionalized Au@AgNW+MWCNTs for VOC sensors) were selectively deposited onto the interdigitated electrodes.

Characterization of the developed sensor

The electrical resistance changes were measured by a digital multimeter (DAQ970A, Keysight) and recorded by the software BenchVue 2018. The capacitance variation was captured by the Capacitive to Digital Converter Evaluation Module (FDC1004EVM, Texas Instruments). The temperature was controlled by a hot plate. Humidity was produced with a wet nitrogen gas stream. VOC gases were generated by bubbling nitrogen gas through the corresponding organic solvents. The concentration of VOC vapors was modulated by MKS mass flow controllers. For VOC sensor measurement, the sensor was exposed to VOC vapors at a fixed concentration for 2 min, followed by pure nitrogen gas purging for another 2 min for baseline recovery. Morphologies of sensing materials were measured by SEM (Thermo Fisher Scientific Quanta 3D FEG), TEM (Thermo Fisher Scientific Talos F200X), and EDS (Thermo Fisher Scientific Super-X EDS with the four silicon drift detectors). Sensors were attached onto the leaf surface using double-sided tape (2477p, 3M) and connected to the data acquisition system with thin copper wires (FIXFANS) and silver adhesive epoxy (MG Chemicals) for interconnection. A commercial sensor device (Amprobe, THWD-5) was used for measuring relative humidity and temperature of the environment. A leaf porometer (Decagon Devices Inc., SC-1 leaf porometer) was used to measure the stomatal conductance, leaf surface humidity, and leaf surface temperature of the tomato plants under various abiotic stress conditions to validate the sensor measurement. For the reproducibility of porometer measurement, two healthy tomato plants (5 to 6 weeks old) for each stress condition were used, and for each plant, three different leaflets were measured to minimize signal variation. In total, six measurements (from six different leaflets) were performed for each stressor, and 12 plants were used for the experiments. For each measurement, the porometer data were collected every 30, 60, or 120 min, and the measurements were continued for 2 to 4 days for different stressors.

Preparation of host tomato plants

Susceptible tomato plants (cv. Mountain Fresh Plus) were grown from seed at the NCSU Phytotron with a combination of natural light and artificial light (14-hour photoperiod) and a 26°C day and 22°C night temperature cycle. Approximately 1 week before the experiment, 5- to 6-week-old plants were transferred to a growth chamber with a 16-hour photoperiod kept at 23°C (both day and night) for the entire experimental period.

One plant was selected for each inoculation. The plant was then placed in an inverted inoculation box lined with moist paper towels to provide water and humidity throughout the experiment.

A. linariae inoculation

An isolate of *A. linariae* (JD1B) was maintained on potato dextrose agar throughout the experiment. To generate conidia, pieces of agar with active *A. linariae* culture were broken up in potato dextrose broth and spread onto sporulation agar (0.2 g of $CaCO_3$, 100 ml of V8 juice, 20 g of Difco Bacto agar, and 1 liter of dH_2O). Plates were incubated at 20°C under constant light for 2 weeks. Conidia production was then stimulated by brushing the plates with a dry sterile cell spreader and incubating at room temperature for 1 to 2 days with the lids ajar in an inoculation box. To harvest conidia, 2 ml of sterile distilled water was added to the plate and brushed with a cell spreader. The liquid was then removed and quantified using a hemocytometer. The conidia solution was diluted to 2000 conidia/ml using distilled water. Four plants were sprayed with 2 ml of the conidia solution over the entire surface of the plant, while four control plants were sprayed with 2 ml of distilled water. Plants were covered with clear plastic bags to maintain humidity. In addition to monitoring by the sensor, visual symptoms were observed daily for 1 week by measuring the percent leaf area diseased (%LAD) using a modified Horsfall-Barratt scale (table S4).

TSWV inoculation

A week before the experiment, a 2-week-old tomato Mountain Fresh seedling, susceptible to TSWV, was placed in a growth chamber at 23°C with a 16-hour light/8-hour dark schedule. The plant in a pot was also enclosed in a plastic container with paper towels soaked in a nutrient solution. As the experiment started, the seedling was inoculated with a wild-type TSWV strain that originated from California using a mechanical leaf-rub method. First, all leaves were sprinkled with carborundum (*39*). Second, several young leaves from TSWV-infected tomatoes were ground in an ice-cold mortar with approximately 5 to 10 ml of sodium sulfite solution (63 mg per 50 ml of tap water) as a buffer. Next, two cotton applicators were repeatedly dipped into the ground tissue mix and rubbed on each leaf using a gloved hand to support the leaf and ensure small wounds were made on the leaf surface. The leaf area with the sensor attached was avoided. Ten minutes after this procedure, the tomato plant was sprayed with DI water to remove the remaining carborundum. The plant was kept enclosed in a controlled chamber for 14 days. Plants were fertilized with nutrient solution three times per week. For the negative control, mock inoculation was performed with healthy leaf tissue, and the experiment schedule was kept the same.

TSWV LAMP assay

At the experiment termination, one young leaf was used for DNA/RNA extraction. Polymeric microneedle patch was pressed on a leaf and rinsed with 60 μl of DI water (*12*). To detect TSWV, 25-μl LAMP reactions with EvaGreen fluorescent and hydroxy naphthol blue colorimetric dye were performed on a Bio-Rad CFX96 real-time machine (*12*). For each reaction, 2 μl of microneedle extraction was used for analysis. For positive controls, we used 2 μl of RNA extracted with Total RNA (Plant) Kit (IBI Scientific) from symptomatic tomato plants maintained in the laboratory. For no template controls, 2 μl of molecular grade DI water was added to the reactions. Positive reactions were detected by green fluorescence with C_t values recorded, as well as by a color change from violet to light blue.

Principal components analysis

We performed PCA, data analysis, and plots in the Project Jupyter platform using Python programming language. Then, we found the centroid of each cluster by using centroid function in the *k*-means clustering approach to calculate the Euclidean distance. In a three-component PCA space, Euclidean distance D was defined as

$$D(p,q) = \sqrt{(p_1 - q_1)^2 + (p_2 - q_2)^2 + (p_3 - q_3)^2}$$

where p and q are known as the centroids of cluster 1 and cluster 2, respectively. The discriminability value (D) is calculated by subtracting the summation of the SDs ($R_{STD,1} + R_{STD,2}$) of a pair of clusters from the corresponding Euclidean distance (E)

$$D = E - (R_{STD,1} + R_{STD,2})$$

Positive discriminability values indicate the cluster separation without overlaps. For four to six sensors, we applied three-component PCA. For three and two sensor combinations, we applied two-component and one-component PCA approaches, respectively. In addition, we calculated the capture variance of each component of PCA and showed them on each axis.

Supplementary Materials

This PDF file includes:

Figs. S1 to S30
Tables S1 to S4
References

View/request a protocol for this paper from *Bio-protocol*.

REFERENCES AND NOTES

1. J. B. Ristaino, P. K. Anderson, D. P. Bebber, K. A. Brauman, N. J. Cunniffe, N. V. Fedoroff, C. Finegold, K. A. Garrett, C. A. Gilligan, C. M. Jones, M. D. Martin, G. K. MacDonald, P. Neenan, A. Records, D. G. Schmale, L. Tateosian, Q. Wei, The persistent threat of emerging plant disease pandemics to global food security. *Proc. Natl. Acad. Sci. U.S.A.* **118**, e2022239118 (2021).
2. E. C. Oerke, Crop losses to pests. *J. Agric. Sci.* **144**, 31–43 (2006).
3. S. Savary, L. Willocquet, S. J. Pethybridge, P. Esker, N. McRoberts, A. Nelson, The global burden of pathogens and pests on major food crops. *Nat. Ecol. Evol.* **3**, 430–439 (2019).
4. B. Cara, J. J. Giovannoni, Molecular biology of ethylene during tomato fruit development and maturation. *Plant Sci.* **175**, 106–113 (2008).
5. M. D. Campos, M. R. Felix, M. Patanita, P. Materatski, C. Caranda, High throughput sequencing unravels tomato-pathogen interactions towards a sustainable plant breeding. *Hortic. Res.* **8**, 171 (2021).
6. M. C. Picanco, L. Bacci, L. B. Crespo, M. M. M. Miranda, J. C. Martins, Effect of integrated pest management practices on tomato production and conservation of natural enemies. *Agric. For. Entomol.* **9**, 327–335 (2007).
7. H. N. Fones, D. P. Bebber, T. M. Chaloner, W. T. Kay, G. Steinberg, S. J. Gurr, Threats to global food security from emerging fungal and oomycete crop pathogens. *Nat. Food* **1**, 332–342 (2020).
8. F. M. Padilla, M. Gallardo, M. T. Pena-Fleitas, R. Souza, R. B. Thompson, Proximal optical sensors for nitrogen management of vegetable crops: A review. *Sensors* **18**, 2083 (2018).
9. V. Singh, A. K. Misra, Detection of plant leaf diseases using image segmentation and soft computing techniques. *Inf. Process. Agric.* **4**, 41–49 (2017).
10. T. T. S. Lew, V. B. Koman, K. S. Silmore, J. S. Seo, P. Gordiichuk, S. Y. Kwak, M. Park, M. C. Y. Ang, D. T. Khong, M. A. Lee, M. B. Chan-Park, N. H. Chua, M. S. Strano, Real-time detection of wound-induced H_2O_2 signalling waves in plants with optical nanosensors. *Nat. Plants* **6**, 404–415 (2020).
11. Z. Li, R. Paul, T. B. Tis, A. C. Saville, J. C. Hansel, T. Yu, J. B. Ristaino, Q. Wei, Non-invasive plant disease diagnostics enabled by smartphone-based fingerprinting of leaf volatiles. *Nat. Plants* **5**, 856–866 (2019).
12. R. Paul, E. Ostermann, Y. Chen, A. C. Saville, Y. Yang, Z. Gu, A. E. Whitfield, J. B. Ristaino, Q. Wei, Integrated microneedle-smartphone nucleic acid amplification platform for in-field diagnosis of plant diseases. *Biosens. Bioelectron.* **187**, 113312 (2021).
13. T. Liu, L. Wang, S. Zuo, C. Yang, Remote sensing dynamic monitoring system for agricultural disaster in Henan province based on multi-source satellite data. *Agric. Sci. Technol.* **14**, 155–161 (2013).
14. D. Tran, F. Dutoit, E. Najdenovska, N. Wallbridge, C. Plummer, M. Mazza, L. E. Raileanu, C. Camps, Electrophysiological assessment of plant status outside a Faraday cage using supervised machine learning. *Sci. Rep.* **9**, 17073 (2019).
15. S. Yao, P. Swetha, Y. Zhu, Nanomaterial-enabled wearable sensors for healthcare. *Adv. Healthc. Mater.* **7**, 1700889 (2018).
16. G. Lee, G. Y. Bae, J. H. Son, S. Lee, S. W. Kim, D. Kim, S. G. Lee, K. Cho, User-interactive thermotherapeutic electronic skin based on stretchable thermochromic strain sensor. *Adv. Sci.* **7**, 2001184 (2020).
17. W. Zhou, S. Yao, H. Wang, Q. Du, Y. Ma, Y. Zhu, Gas-permeable, ultrathin, stretchable epidermal electronics with porous electrodes. *ACS Nano* **14**, 5798–5805 (2020).
18. N. Lu, D. H. Kim, Flexible and stretchable electronics paving the way for soft robotics. *Soft Robot.* **1**, 53–62 (2014).
19. Y. Lu, K. Xu, L. Zhang, M. Deguchi, H. Shishido, T. Arie, R. Pan, A. Hayashi, L. Shen, S. Akita, K. Takei, Multimodal plant healthcare flexible sensor system. *ACS Nano* **14**, 10966–10975 (2020).
20. H. Yin, Y. Cao, B. Marelli, X. Zeng, A. J. Mason, C. Cao, Soil sensors and plant wearables for smart and precision agriculture. *Adv. Mater.* **33**, 2007764 (2021).
21. G. Lee, Q. Wei, Y. Zhu, Emerging wearable sensors for plant health monitoring. *Adv. Funct. Mater.* **31**, 2106475 (2021).
22. F. Brilli, F. Loreto, I. Baccelli, Exploiting plant volatile organic compounds (VOCs) in agriculture to improve sustainable defense strategies and productivity of crops. *Front. Plant Sci.* **10**, 264 (2019).
23. M. Haworth, C. Elliott-Kingston, J. C. McElwain, Stomatal control as a driver of plant evolution. *J. Exp. Bot.* **62**, 2419–2423 (2011).
24. J. M. Nassar, S. M. Khan, D. R. Villava, M. M. Nour, A. S. Almuslem, M. M. Hussain, Compliant plant wearables for localized microclimate and plant growth monitoring. *npj Flex. Electron.* **2**, 24 (2018).
25. Y. Zhao, S. Gao, J. Zhu, J. Li, H. Xu, K. Xu, H. Cheng, X. Huang, Multifunctional stretchable sensors for continuous monitoring of long-term leaf physiology and microclimate. *ACS Omega* **4**, 9522–9530 (2019).
26. Z. Li, Y. Liu, O. Hoosain, R. Paul, S. Yao, S. Wu, J. B. Ristaino, Y. Zhu, Q. Wei, Real-time monitoring of plant stresses via chemiresistive profiling of leaf volatiles by a wearable sensor. *Matter* **4**, 2553–2570 (2021).
27. M. Yang, Z. D. Hood, X. Yang, M. Chi, Y. Xia, Facile synthesis of Ag@Au core–sheath nanowires with greatly improved stability against oxidation. *Chem. Commun.* **53**, 1965–1968 (2017).
28. R. M. C. Jansen, J. Wildt, I. F. Kappers, H. J. Bouwmeester, J. W. Hofstee, E. J. van Henten, Detection of diseased plants by analysis of volatile organic compound emission. *Annu. Rev. Phytopathol.* **49**, 157–174 (2011).
29. C. Tasaltin, F. Basarir, Preparation of flexible VOC sensor based on carbon nanotubes and gold nanoparticles. *Sens. Actuators B Chem.* **194**, 173–179 (2014).
30. L. Liu, X. Ye, K. Wu, R. Han, Z. Zhou, T. Cui, Humidity sensitivity of multi-walled carbon nanotube networks deposited by dielectrophoresis. *Sensors* **9**, 1714–1721 (2009).
31. Z. Cui, F. R. Poblete, Y. Zhu, Tailoring the temperature coefficient of resistance of silver nanowire nanocomposites and their application as stretchable temperature sensors. *ACS Appl. Mater. Interfaces* **11**, 17836–17842 (2019).
32. J. Bang, W. S. Lee, B. Park, H. Joh, H. K. Woo, S. Jeon, J. Ahn, C. Jeong, T. I. Kim, S. J. Oh, Highly sensitive temperature sensor: Ligand-treated Ag nanocrystal thin films on PDMS with thermal expansion strategy. *Adv. Funct. Mater.* **29**, 1903047 (2019).
33. C. Sapsanis, U. Buttner, H. Omran, Y. Belmabkhout, O. Shekhah, M. Eddaoudi, K. N. Salama, A nafion coated capacitive humidity sensor on a flexible PET substrate, in *2016 IEEE 59th International Midwest Symposium on Circuits and Systems (MWSCAS)* (2016), pp. 1–4.
34. A. Karimi, Y. Wang, T. Cselle, M. Morstein, Fracture mechanisms in nanoscale layered hard thin films. *Thin Solid Films* **420-421**, 275–280 (2002).
35. J. Wang, X.-h. Wang, X.-d. Wang, Study on dielectric properties of humidity sensing nanometer materials. *Sensors Actuators B Chem.* **108**, 445–449 (2005).
36. E. Latkowska, Z. Lechowski, J. Bialczyk, J. Pilarski, Photosynthesis and water relations in tomato plants cultivated long-term in media containing (+)-usnic acid. *J. Chem. Ecol.* **32**, 2053–2066 (2006).
37. O. Halperin, A. Gebremedhin, R. Wallach, M. Moshelion, High-throughput physiological phenotyping and screening system for the characterization of plant–environment interactions. *Plant J.* **89**, 839–850 (2017).

38. R. Munns, D. P. Schachtman, A. G. Condon, The significance of a two-phase growth response to salinity in wheat and barley. *Aust. J. Plant Physiol.* **22**, 561–569 (1995).
39. P. Nachappa, J. Challacombe, D. C. Margolies, J. R. Nechols, A. E. Whitfield, D. Rotenberg, Tomato spotted wilt virus benefits its thrips vector by modulating metabolic and plant defense pathways in tomato. *Front. Plant Sci.* **11**, 575564 (2020).
40. N. Bessadat, R. Berruyer, B. Hamon, N. Bataille-Simoneau, S. Benichou, M. Kihal, D. E. Henni, P. Simoneau, *Alternaria* species associated with early blight epidemics on tomato and other *Solanaceae* crops in northwestern Algeria. *Eur. J. Plant Pathol.* **148**, 181–197 (2017).
41. M. Wang, N. Ling, X. Dong, Y. Zhu, Q. Shen, S. Guo, Thermographic visualization of leaf response in cucumber plants infected with the soil-borne pathogen *Fusarium oxysporum* f. sp. *cucumerinum*. *Plant Physiol. Biochem.* **61**, 153–161 (2012).
42. V. Ramegowda, M. Senthil-Kumar, The interactive effects of simultaneous biotic and abiotic stresses on plants: Mechanistic understanding from drought and pathogen combination. *J. Plant Physiol.* **176**, 47–54 (2015).
43. K. M. Gold, P. A. Townsend, E. R. Larson, I. Herrmann, A. J. Gevens, Contact reflectance spectroscopy for rapid, accurate, and nondestructive *Phytophthora infestans* clonal lineage discrimination. *Phytopathology* **110**, 851–862 (2020).
44. A. Leal-Junior, L. Avellar, A. Frizera, C. Marques, Smart textiles for multimodal wearable sensing using highly stretchable multiplexed optical fiber system. *Sci. Rep.* **10**, 13867 (2020).
45. I. T. Jolliffe, J. Cadima, Principal component analysis: A review and recent developments. *Phil. Trans. R. Soc. A* **374**, 20150202 (2016).
46. P. Aghdaie, B. Chaudhary, S. Soleymani, J. Dawson, N. M. Nasrabadi, Detection of morphed face images using discriminative wavelet sub-bands. arXiv:2106.08565 [Preprint] [cs.CV]. (16 June 2020).
47. S. Raza, H. K. Smith, G. J. J. Clarkson, G. Taylor, A. J. Thompson, J. Clarkson, N. M. Rajpoot, Automatic detection of regions in spinach canopies responding to soil moisture deficit using combined visible and thermal imagery. *PLOS ONE* **9**, e97612 (2014).
48. Y. Liu, M. Zheng, B. O'Connor, J. Dong, Y. Zhu, Curvilinear soft electronics by micromolding of metal nanowires in capillaries. *Sci. Adv.* **8**, 6996 (2022).
49. A. C. Castonguay, N. Yi, B. Li, J. Zhao, H. Li, Y. Gao, N. N. Nova, N. Tiwari, L. D. Zarzar, H. Cheng, Direct laser writing of microscale metal oxide gas sensors from liquid precursors. *ACS Appl. Mater. Interfaces* **14**, 28163–28173 (2022).
50. R. Yang, W. Zhang, N. Tiwari, H. Yan, T. Li, H. Cheng, Multimodal sensors with decoupled sensing mechanisms. *Adv. Sci.* **9**, 2202470 (2022).
51. S. Zhang, J. Zhu, Y. Zhang, Z. Chen, C. Song, J. Li, N. Yi, D. Qiu, K. Guo, C. Zhang, T. Pan, Y. Lin, H. Zhou, H. Long, H. Yang, H. Cheng, Standalone stretchable RF systems based on asymmetric 3D microstrip antennas with on-body wireless communication and energy harvesting. *Nano Energy* **96**, 107069 (2022).
52. N. Yi, Y. Gao, A. L. Verso Jr., J. Zhu, D. Erdely, C. Xue, R. Lavelle, H. Cheng, Fabricating functional circuits on 3D freeform surfaces via intense pulsed light-induced zinc mass transfer. *Mater. Today* **50**, 24–34 (2021).
53. K. E. Korte, S. E. Skrabalak, Y. Xia, Rapid synthesis of silver nanowires through a CuCl- or CuCl2-mediated polyol process. *J. Mater. Chem.* **18**, 437–441 (2008).
54. S. M. Khan, S. F. Shaikh, N. Qaiser, M. M. Hussain, Flexible lightweight CMOS-enabled multisensory platform for plant microclimate monitoring. *IEEE Trans. Electron Devices* **65**, 5038–5044 (2018).
55. J. J. Kim, L. K. Allison, T. L. Andrew, Vapor-printed polymer electrodes for long-term, on-demand health monitoring. *Sci. Adv.* **5**, 463 (2019).
56. D. Lo Presti, S. Cimini, C. Massaroni, R. D'Amto, M. A. Caponero, L. De Gara, E. Schena, Plant wearable sensors based on FBG technology for growth and microclimate monitoring. *Sensors* **21**, 6327 (2021).
57. W. Ahmad, B. Jabbar, I. Ahmad, B. M. Jan, M. M. Stylianakis, G. Kenanakis, R. Ikram, Highly sensitive humidity sensors based on polyethylene oxide/CuO/multi walled carbon nanotubes composite nanofibers. *Materials* **14**, 1037 (2021).
58. W. P. Shih, L. C. Tsao, C. W. Lee, M. Y. Cheng, C. Chang, Y. J. Yang, K. C. Fan, Flexible temperature sensor array based on a graphite-polydimethylsiloxane composite. *Sensors* **10**, 3597–3610 (2010).
59. A. Cusano, M. Consales, A. Crescitelli, M. Penza, P. Aversa, P. Delli Veneri, M. Giordano, Charge transfer effects on the sensing properties of fiber optic chemical nano-sensors based on single-walled carbon nanotubes. *Carbon* **47**, 782–788 (2009).

Acknowledgments: We also thank A. Locke for providing the leaf porometer device. **Funding:** We gratefully acknowledge the funding support from the NCSU Game-Changing Research Incentive Program for the Plant Science Initiative (GRIP4PSI), USDA (no. 2019-67030-29311), USDA APHIS Farm Bill grant (no. 3.0096), and NSF (nos. 1728370 and 2134664). **Author contributions:** G.L., Y.Z., and Q.W. designed and initiated the project. Y.L and O.H. synthesized and characterized AgNW, Au@AgNW, and functionalized Au@AgNW. G.L. fabricated the multimodal wearable sensor and performed on-plant measurements. H.W. characterized the morphology of sensing materials. A.C.S., T.S., J.B.R., and A.E.W. grew the tomato plants and performed the inoculation of different pathogens and LAMP tests. S.J. conducted PCA of the real-time sensor data. R.P. helped with the plant pathogen test in the laboratory. D.R. provided valuable discussion on the experimental design and results analysis. G.L., Y.Z., and Q.W. wrote the manuscript. All the authors read and revised the manuscript. **Competing interests:** The authors declare that they have no competing interests. **Data and materials availability:** All data needed to evaluate the conclusions in the paper are present in the paper and/or the Supplementary Materials.

Submitted 1 August 2022
Accepted 16 March 2023
Published 12 April 2023
10.1126/sciadv.ade2232